MALADAPTIVE IMMUNE-FIBROTIC AXIS DRIVES IMPAIRED LONG BONE REGENERATION UNDER MECHANICAL INSTABILITY

Matthew D. Patrick[1], Jaimo Ahn[2], Kurt D. Hankenson[3], and Ramkumar T. Annamalai[1]*

[1]Department of Biomedical Engineering, University at Buffalo, Buffalo, NY 14260

[2]Department of Orthopedics, Emory University and Grady Memorial Hospital, Atlanta, GA 30303

[3]Department of Orthopedic Surgery, University of Michigan, MI 48109

*Author Correspondence:

Ramkumar T. Annamalai, PhD

219 Biomedical Research Building

University at Buffalo, NY 14214

Email: rtiruvan@buffalo.edu

Short Title: *Mechanical Instability Drives Fibrotic Bone Healing*

***Keywords*:** Hypertrophic Nonunion, Fracture, Interfragmentary strain, Delayed Healing, Biomarker

ABSTRACT

Delayed and nonhealing fractures, affecting 5–10% of incidents, result in prolonged disability and reduced quality of life for the patient. While acute inflammation initiates healing, dysregulated immune responses exacerbate bone resorption and fibrosis. Current animal models fail to replicate mechanical instability, the primary driver of clinical hypertrophic nonunion, limiting translational insights. Here, we engineer a murine delayed-healing model using tunable intramedullary nails to impose controlled interfragmentary strains, mimicking human hypertrophic nonunion. High-strain fractures (15-30%) generated larger calluses with delayed ossification, 2.9-fold increase in fibrotic tissue (p = 0.0099), and inferior biomechanical strength (stiffness: 1.6-fold lower, p = 0.024) compared to low-strain controls (<5%). Spatial transcriptomics revealed persistent fibrotic niches in high-strain calluses enriched with fibroblast-associated genes (*Pdgfrb*, *Lgals3*) alongside dysregulated macrophage-osteoclast signaling (*Spp1*, *Mmp9*). Systemic immune profiling revealed CD206+ macrophages and CD25+ T-regulatory cells as predictive biomarkers, with early polarization determining long-term outcomes (R = 0.72, p = 0.004). Multivariate modeling linked delayed healing to persistent CD8+ T cells and deficient Treg recruitment, perpetuating inflammation. These findings establish mechanical instability as a catalyst for pathological immune-stromal crosstalk and provide a platform for mechano-informed immunotherapies. Our work redefines hypertrophic nonunion as a disorder of mechano-immunology, offering novel diagnostic and therapeutic strategies to mitigate fibrosis and restore regeneration.

Teaser: Mechanical strain hijacks immune signaling to induce fibrosis and block bone regeneration in unstable fractures.

A. INTRODUCTION

Fractures with delayed healing or nonunion remain a life-altering clinical challenge, affecting 5–10% of the 8 million annual fractures in the U.S., with profound impacts on patient morbidity and quality of life that can surpass chronic conditions like stroke, diabetes, and heart failure[1-3]. Currently, there is no standardized method for determining nonunions at early stages, and it takes 6-9 months from injury or fixation for definitive diagnosis[4]. The FDA defines a nonunion as a fracture that has not healed for at least 9 months with no progressive signs of healing for 3 consecutive months[5]. In the setting of clear clinical gaps, the biomechanical mechanism by which nonunions develop is not well understood, limiting our ability to address them scientifically

Among these cases, hypertrophic nonunion, driven by mechanical instability as defined by the widely accepted aseptic nonunion classification system[6], is the most prevalent yet least understood subtype[7,8]. Unlike atrophic nonunions, which arise from biological deficiencies, hypertrophic nonunions develop in mechanically unstable environments where excessive interfragmentary strain disrupts the transition from provisional fibrotic and cartilaginous tissue to mineralized bone[7,8]. Despite its clinical prevalence, research has been hampered by the lack of animal models that recapitulate the mechanopathology of human hypertrophic nonunion. This leaves critical gaps in understanding how mechanical strain drives fibrosis and immune dysregulation to impair healing, which in turn limits our ability to address it therapeutically for clinical benefit.

Fibrosis as a Mechano-Immunological Barrier

Bone uniquely regenerates without scarring under optimal conditions[89], but mechanical instability disrupts this process. In cases of fracture nonunion and delayed union, fibrotic tissues frequently develop in the fracture gaps of long bones, significantly impairing function and quality of life[10]. Conventionally, fibrotic tissues are associated with the atrophic form of nonunion due to the critical size of the defect. But mechanical instability, the most common cause of nonunion in clinical practice[11], can also induce fibrosis. According to the strain theory[12-14], tolerance to local strain dictates the type of tissue developing in the fracture site. Simulations and models of tissue differentiation suggest that interfragmentary strains >15% induce fibrous tissue formation, while <5% permits direct bone healing[15]. As the fracture heals, the callus tissue gets stiffer over time due to cell infiltration and ECM deposition, and the strain gradually minimizes until it is conducive to ossification. In hypertrophic nonunion, persistent high strain (15-30%) traps the callus in a fibrotic state, yet the molecular drivers of this pathology remain unclear. Fibrosis, marked by aberrant extracellular matrix (ECM) deposition, is increasingly recognized as a hallmark of delayed healing in unstable fractures[16]. Traditional animal models, which impose biological deficits or withhold treatment[17] fail to replicate strain-driven fibrosis, leaving critical gaps in understanding macrophage-fibroblast crosstalk and immune dysregulation.

A Clinically Relevant Model of Strain-Driven Fibrosis

To address this, we developed a murine delayed-healing model that recapitulates clinical hypertrophic nonunion through controlled interfragmentary strain. Building on an established blunt-trauma fracture model[18,19], we stabilized femoral fractures immediately with tunable intramedullary nails to impose low (<5%) or high (15-30%) strain microenvironments. Unlike prior approaches that withhold treatment[17], our system mirrors clinical reality while isolating strain as the driver of pathology. High

strain (15-30%) upregulated thrombospondins (THBS1/2) in macrophages and syndecan-4 (SDC4) in fibroblasts, a ligand-receptor pair known to activate TGF-β and drive fibrosis in other tissues[20]. Concurrently, *Lgals3*+ macrophages, associated with chronic fibrosis in muscle and liver, dominated fibrotic calluses, secreting *Spp1* to recruit fibroblasts and *Pdgfrb* to sustain ECM remodeling. This maladaptive crosstalk creates a self-reinforcing fibrotic loop, diverting healing from ossification to scar-like tissue. Systemic immune shifts further underscored the mechano-immunological axis. High-strain fractures showed prolonged CD8+ T-cell elevation and reduced Tregs, correlating with poor healing. In contrast, early CD206+ macrophage and Treg expansion in low-strain fractures predicted successful regeneration. These findings align with clinical reports of altered leukocyte kinetics in nonunion patients[17] and position immune polarization as a therapeutic target.

Our work redefines hypertrophic nonunion as a disorder of maladaptive mechano-immunology, driven by THBS-SDC4 signaling and Lgals3+ macrophage-mediated fibrosis. The identification of CD206+ macrophages and Tregs as biomarkers offers a path for early diagnosis, while targeting fibrotic pathways (e.g., THBS inhibition) could restore regenerative balance. By bridging biomechanics and immunology, this model provides a platform to develop therapies for the millions affected by delayed fracture healing worldwide.

B. RESULTS

1. Modulating Interfragmentary Strain via Customized Intramedullary Nail Stiffness

To investigate the impact of mechanical instability on fracture healing, we engineered intramedullary (IM) nails from superelastic nitinol alloy (NiTi) with tailored stiffness profiles (3–30 N/mm, Supplementary **Fig. S1**). Using three-point flexure testing, we identified two distinct nail configurations: a low-stiffness nail (2.7 ± 0.05 N/mm) designed to permit high interfragmentary strain (>15%) and a high-stiffness nail (16.5 ± 0.41 N/mm) to restrict strain to <5% under physiological loading (**Fig. 1A**). Compared to standard titanium nail (stiffness = 44 ± 3.3 N/mm, diameter = 0.51 mm) our previous studies showed an identical healing profile to the high-stiffness nail, leading us to choose it as our control group. Femurs were reamed with 25- or 27-gauge hypodermic needles to ensure precise fixation of the low- and high-stiffness nails, respectively, followed by transverse fracture induction and stabilization.

Biomechanical validation revealed that stabilized femurs exhibited slightly reduced stiffness compared to standalone nails (low-stiffness group: 1.96 ± 0.41 N/mm vs. nail alone: 2.7 N/mm; high-stiffness group: 13.21 ± 1.53 N/mm vs. nail alone: 16.5 N/mm; **Fig. 1B**). Despite this attenuation, physiological loads (1.5–3 N, approximating murine hindlimb forces) generated bending strains of 15.1 ± 1.4% in low-stiffness nails and 3.3 ± 1.4% in high-stiffness nails (**Fig. 1C**), successfully replicating the strain thresholds associated with fibrous tissue formation (>15%) and direct bone healing (<5%). This established a robust platform to dissect strain-dependent healing outcomes in subsequent analyses.

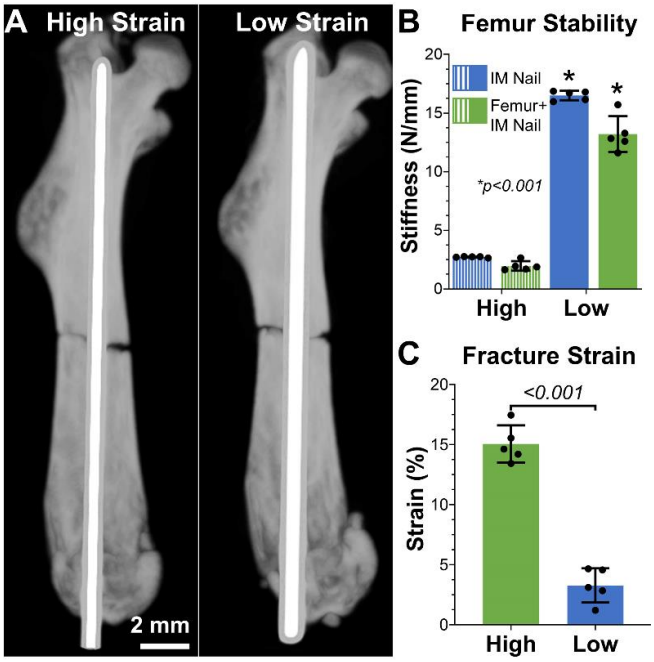

Figure 1. Intramedullary Nail Stiffness Modulates Interfragmentary Strain During Fracture Healing. ***(A)*** *Representative maximum-intensity projection microCT scans of murine femurs stabilized with low- or high-stiffness intramedullary (IM) nails.* ***(B)*** *Stiffness of standalone nitinol nails versus nails implanted in fractured femurs (n = 5 per group).* ***(C)*** *Flexural strain at the fracture site under physiological loads (n = 5 per group, mean ± SD).*

2. Interfragmentary Strain Governs Callus Morphology and Composition

To assess strain-dependent healing outcomes, transverse femoral fractures in 22-week-old mice (n = 12/group) were stabilized with low- (<5%) or high-stiffness (>15%) nails. At 3 weeks post-fracture, microCT analysis revealed stark morphological differences: high-strain fractures formed larger calluses with 1.7-fold greater tissue volume (TV, $p = 0.003$) and 1.6-fold higher bone volume (BV, $p < 0.001$) compared to low-strain controls (**Fig. 2A–C, 2D–E, Table.1**). Mineralized content in high-strain calluses increased by 1.8-fold ($p < 0.001$, **Fig. 2F**), consistent with clinical hypertrophic nonunion patterns[11]. However, callus bone volume fraction (BV/TV) and mineral density (BMD) showed no significant differences between groups (**Fig. 2G–H**), indicating that mechanical instability drives aberrant callus expansion without altering mineralization efficiency.

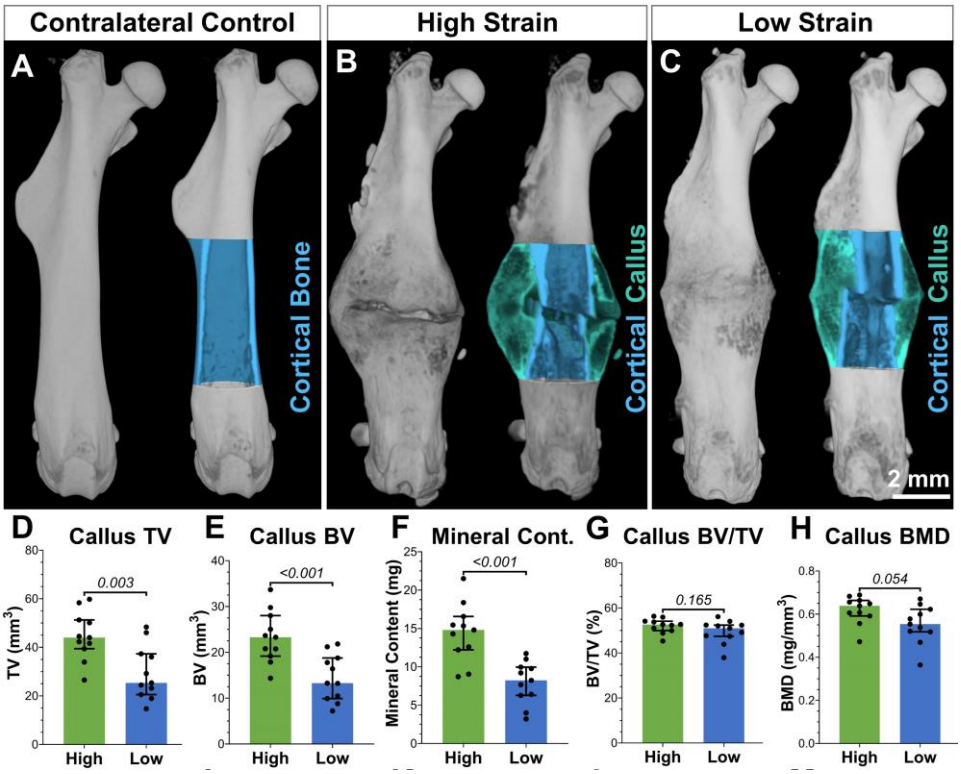

Figure 2. Interfragmentary Strain Dictates Callus Morphology and Composition at 3 Weeks Post-Fracture. *(**A**) Representative 3D microCT reconstructions of contralateral uninjured femurs (control). (B) High-strain group (15% interfragmentary strain) and (C) Low-strain group (<5% interfragmentary strain), with transverse cross-sections highlighting the fracture site (volume of interest: ±2.5 mm from the fracture line). Cortical bone (light blue) and callus tissue (teal) are demarcated. (D–F) Quantitative analysis of callus tissue volume (TV), bone volume (BV), and mineral content (MC) in high- vs. low-strain groups (n = 12 per group; mean ± SD; significance defined as < 0.05, unpaired t-test).*

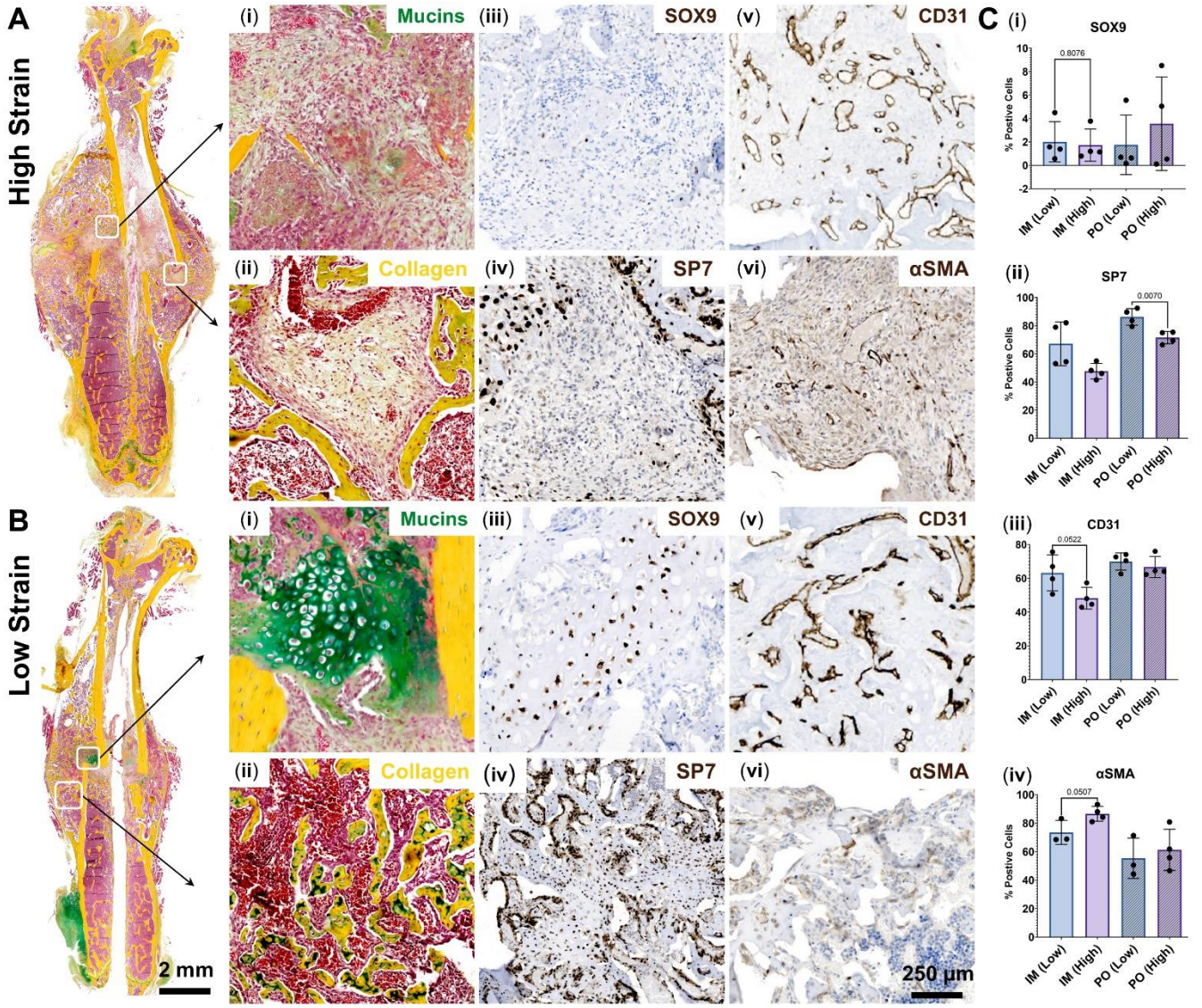

Figure 3. Interfragmentary Strain Modulates Endochondral Ossification and Fibrotic Remodeling. *(**A**) High-strain (15% interfragmentary strain) and (**B**) Low-strain (<5% interfragmentary strain) groups at 3 weeks post-fracture. Representative Movat's pentachrome staining (i–ii) and immunohistochemistry (IHC) of fracture calluses. (i) High-strain callus showing fibrotic tissue (yellow collagen, red fibrin) and reduced chondrogenic areas (blue mucins). (ii) Low-strain callus with mature woven bone (yellow collagen) and minimal fibrosis. (iii) SOX9+ chondrocytes (brown) and (iv) SP7+ osteoblasts (brown) highlight lineage-specific activity. (v) CD31/PECAM+ endothelial cells (brown) indicate vascularization. (vi) α-SMA+ fibrotic regions (brown) dominate high-strain calluses. Scale bars: 500 µm (i–ii), 100 µm (iii–vi). C (i-iv) Quantification of IHC as a percentage of positive cells in the intermedullary (IM) and periosteal (PO) callus under high and low strain conditions (n = 3-4 per group, mean ± SD).*

Histological analysis further delineated strain-dependent healing mechanisms. Movat's Pentachrome staining of week-3 femurs revealed high-strain calluses were dominated by vascularized fibrotic tissue (collagen: yellow; fibrin/muscle: red) with minimal chondrogenic regions (mucins: blue), while low-strain calluses exhibited mature woven bone with robust collagen deposition (**Fig. 3A(i–ii**),

B(i–ii)). Immunohistochemical analysis identified regions of chondrogenesis (SOX9+), osteoblast activity (SP7+), vascularization (CD31+), and myofibroblast activation (α-SMA+) within both high- and low-strain fracture calluses (Fig. 3A(i–iv), 3B(i–iv)). Quantification revealed comparable levels of SOX9+ chondrogenic cells between strain groups across both the intramedullary (IM) and periosteal (PO) callus regions (Fig. 3C(i)). In contrast, SP7+ osteoblast activity was elevated in the low-strain group in both IM and PO compartments (Fig. 3C(ii)). CD31+ endothelial staining indicated similar levels of vascularization in the PO callus, although a downward trend was observed in the IM region under high strain (Fig. 3C(iii)). Notably, α-SMA+ myofibroblast accumulation was increased in the IM region of high-strain calluses, with comparable levels in the PO region across groups (Fig. 3C(iv)), suggesting localized fibrotic remodeling under elevated mechanical load.

Picrosirius red staining combined with polarized light imaging revealed a 2.9-fold increase ($p = 0.0099$) in the fibrotic area within high-strain calluses compared to low-strain controls (**Fig. 4A(i–ii), B(i–ii)**). Polarized light microscopy further demonstrated dense, parallel-aligned fibrillar collagen bundles, a hallmark of mature fibrosis, in high-strain groups, contrasting with the disordered collagen network in low-strain calluses (**Fig. 4A(iii), B(iii)**). Spatial transcriptomics localized enhanced *Col3a1* expression to fibrotic regions of high-strain calluses (**Fig. 4A(iv), B(iv)**), corroborating the molecular signature of pathological ECM remodeling. Together, these findings establish that elevated interfragmentary strain drives collagen dysregulation and fibrosis, impairing functional bone healing, while mechanical stability promotes ossification and regenerative repair.

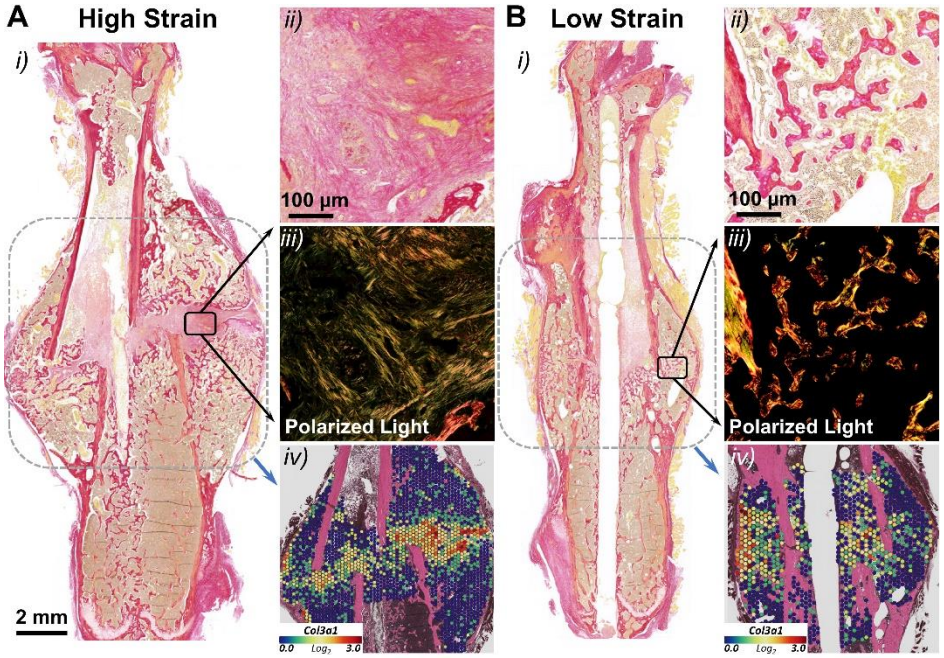

Figure 4. Interfragmentary Strain Drives Fibrotic Remodeling Through Collagen Reorganization and Col3a1 Expression. ***(A)*** *High-strain (15% interfragmentary strain) and* ***(B)*** *Low-strain (<5% interfragmentary strain) groups at 3 weeks post-fracture.* ***(i)*** *Picrosirius red staining (brightfield) identifies fibrotic collagen-rich regions (red).* ***(ii)*** *High-magnification views highlight dense collagen deposition.* ***(iii)*** *Polarized light imaging reveals parallel-aligned fibrillar collagen (bright birefringence) in high-strain calluses, indicative of mature fibrosis, versus disorganized collagen in low-strain groups.* ***(iv)*** *Spatial transcriptomics*

maps show elevated Col3a1 expression (red-purple) in fibrotic regions of high-strain calluses. Scale bars: 2 mm (i), 100 μm (ii–iv).

3. Mechanical Strain Activates Fibrogenic Pathways Through Transcriptional Reprogramming and Cellular Crosstalk

Spatial transcriptomics of week-3 calluses revealed distinct cellular niches shaped by interfragmentary strain (**Fig. 5A**). Unsupervised clustering of gene expression profiles identified fibroblast-rich regions comprising 5.79% of high-strain calluses, a 14-fold increase over low-strain controls (0.39%, **Fig. 5B**). These fibroblast-dense zones spatially overlapped with picrosirius red-positive fibrillar collagen deposits (**Fig. 4A**), confirming their fibrotic identity. High-strain calluses also exhibited a 1.7-fold elevation in osteoclast-rich areas (11.58% vs. 6.96% in low-strain, **Fig. 5C**), with osteoclasts localizing adjacent to fibroblast clusters, suggesting coupled remodeling of fibrotic and mineralized matrices.

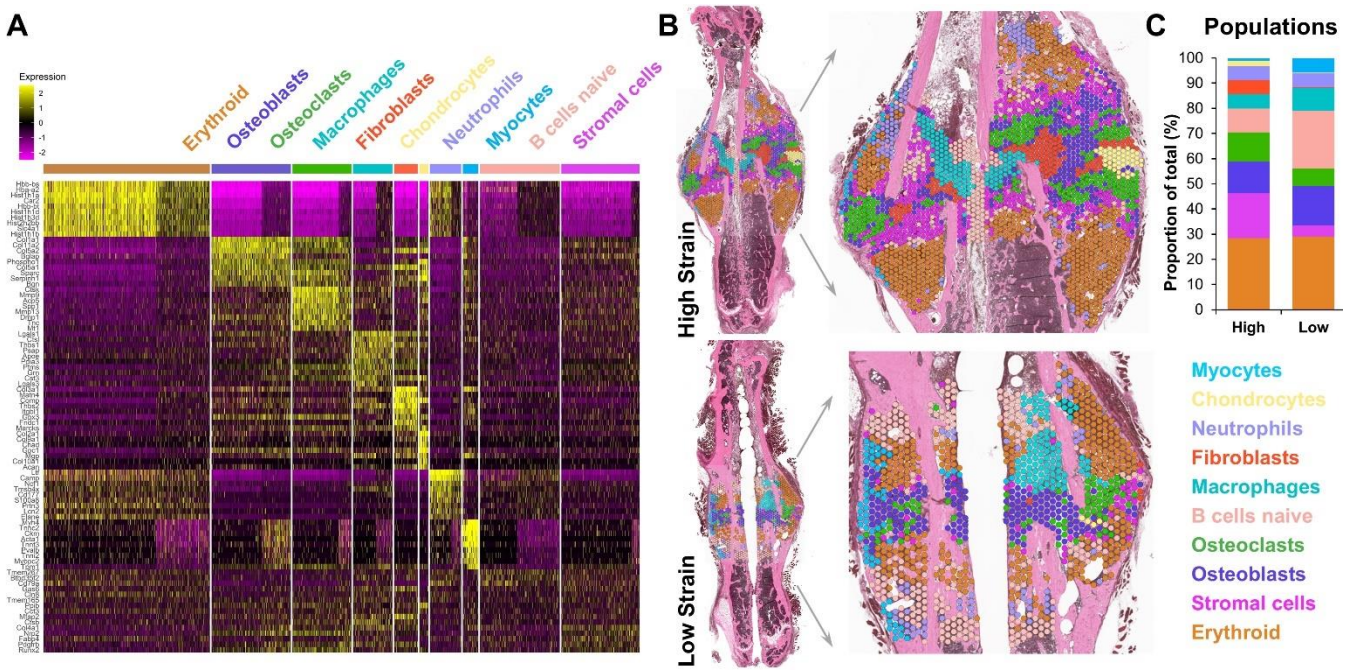

Figure 5. Mechanical Strain Induces Fibroblast-Osteoclast Co-Localization in Fibrotic Callus Niches. *(A) Heatmap of the top 10 differentially expressed genes across spatial transcriptomics clusters. (B) Histological sections of high-strain (15% interfragmentary strain, top) and low-strain (<5% interfragmentary strain, bottom) calluses overlaid with spatial transcriptomics clusters (STclusters). Fibroblast-rich regions (STcluster 2, teal) in high-strain calluses overlap with picrosirius red-positive fibrotic zones (Fig. 4A). (C) Cellular composition analysis reveals a 14-fold increase in fibroblast-rich areas (5.79% vs. 0.39%, $p < 0.001$) and 1.7-fold more osteoclast-rich regions (11.58% vs. 6.96%, $p < 0.01$) in high-strain versus low-strain calluses.*

Despite analogous spatial positioning of cellular niches in high- and low-strain calluses (**Fig. 6A**), transcriptional profiles diverged markedly. Fibrosis-associated genes (*Mmp9, Spp1, Pdgfrb, Lgals3*) mirrored patterns observed in pulmonary and hepatic fibrosis (**Fig. 6B**). High-strain osteoclasts exhibited upregulated *Mmp9* (1.03-fold, $p < 0.0001$), a collagenase linked to pathological matrix degradation, while macrophage-rich regions showed elevated *Spp1* (osteopontin, 0.93-fold), *Pdgfrb* (0.75-fold), and *Lgals3* (galectin-3, 0.58-fold; $p < 0.0137$), key mediators of fibroblast activation and ECM stiffening. Macrophage-

fibroblast proximity in high-strain calluses (**Fig. 6B**) suggested paracrine crosstalk, further supported by UMAP clustering revealing distinct fibrotic transcriptional signatures (**Fig. 6C–D**).

Gene Ontology (GO) enrichment analysis of differentially expressed genes highlighted pathways central to fibroblast proliferation (*PDGF* signaling) and ECM organization (collagen fibril assembly), with macrophages as primary contributors (**Fig. 6E, Tables 2–3**). Osteoclasts and osteoblasts shared enrichment in extracellular matrix disassembly and ossification pathways, respectively, underscoring their dual role in matrix remodeling. These findings position mechanical strain as a catalyst for maladaptive immune-stromal interactions which sustains fibrosis and impedes functional repair.

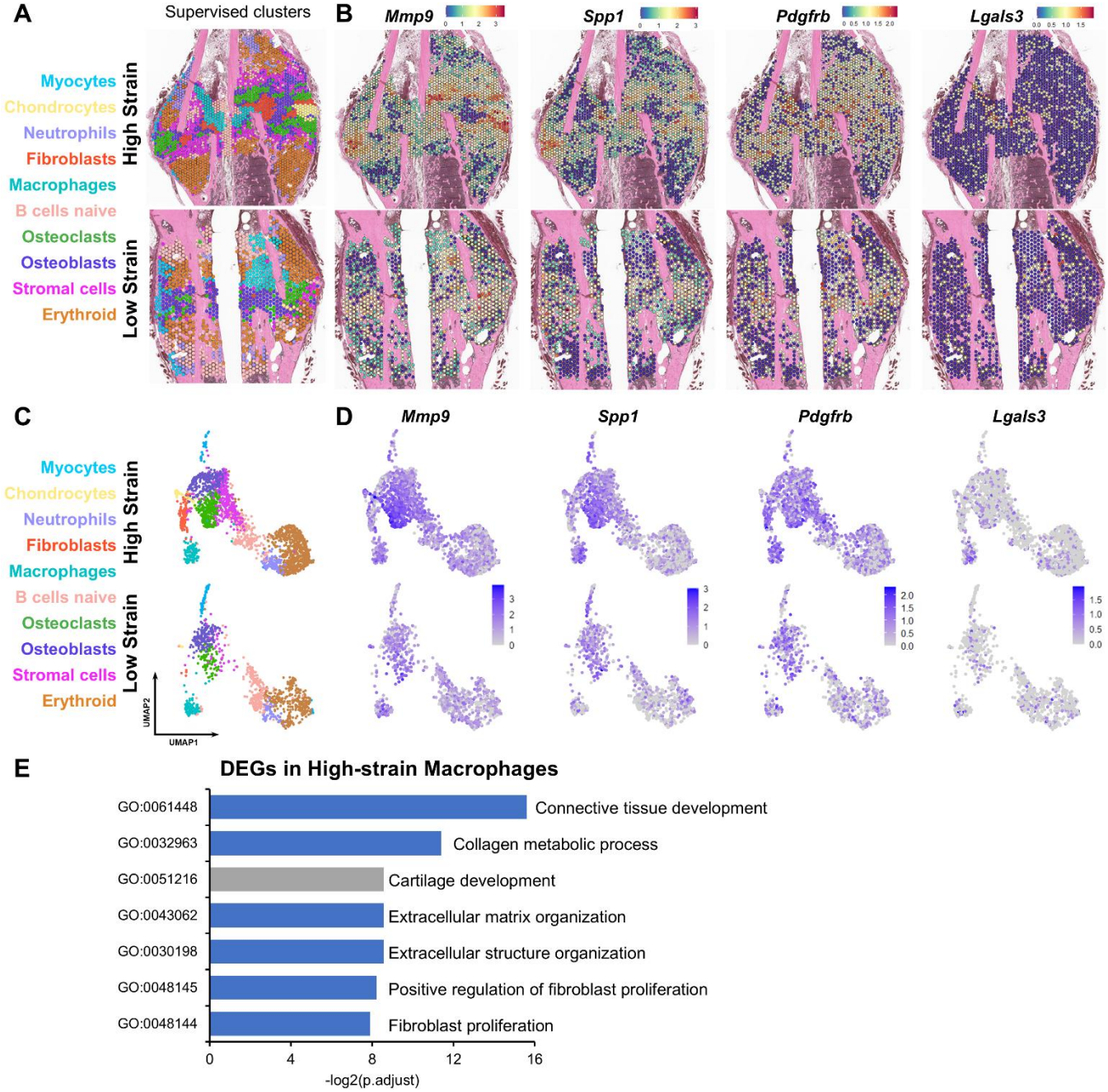

Figure 6. Strain-Dependent Transcriptional Reprogramming Drives Fibrotic Remodeling. *(**A**) Histological sections of high-strain (15% interfragmentary strain, top) and low-strain (5% interfragmentary strain, bottom) calluses with overlaid spatial transcriptomics clusters. (**B**) Spatial expression maps of fibrosis-associated genes (Mmp9, Spp1, Pdgfrb, Lgals3) in high- and low-strain groups. (**C**) UMAP plots of cell clusters colored by type. (**D**) UMAP projections showing expression levels of fibrotic genes, with intensity representing expression levels. (**E**) Gene Ontology (GO) analysis of biological processes enriched due to differentially upregulated genes in high-strain macrophages.*

CellChat analysis revealed enhanced communication between fibroblasts, macrophages, and osteoclasts in high-strain calluses. High-strain groups exhibited globally elevated cellular communication compared to low-strain controls, with fibroblasts, macrophages, and osteoclasts emerging as hubs for incoming and outgoing signals (**Fig.7A**). Pathway analysis identified 16 mechano-sensitive pathways, including *TGFβ, ncWNT, PDGF, THBS, FN1, SPP1, TENASCIN*, and *COLLAGEN*. Notably, the *TENASCIN* and *THBS* pathways exhibited the most pronounced activation with the highly differential signaling (**Fig.7B**). Macrophages in high-strain calluses communicated via *Thbs1/2* and *Comp* ligands targeting fibroblast *Sdc4* receptors, while osteoclasts utilized *Tnc* and *Comp* to engage fibroblasts receptors (**Fig. 7C–D**). These interactions were totally absent in low-strain calluses, underscoring strain-dependent modulation of cellular crosstalk.

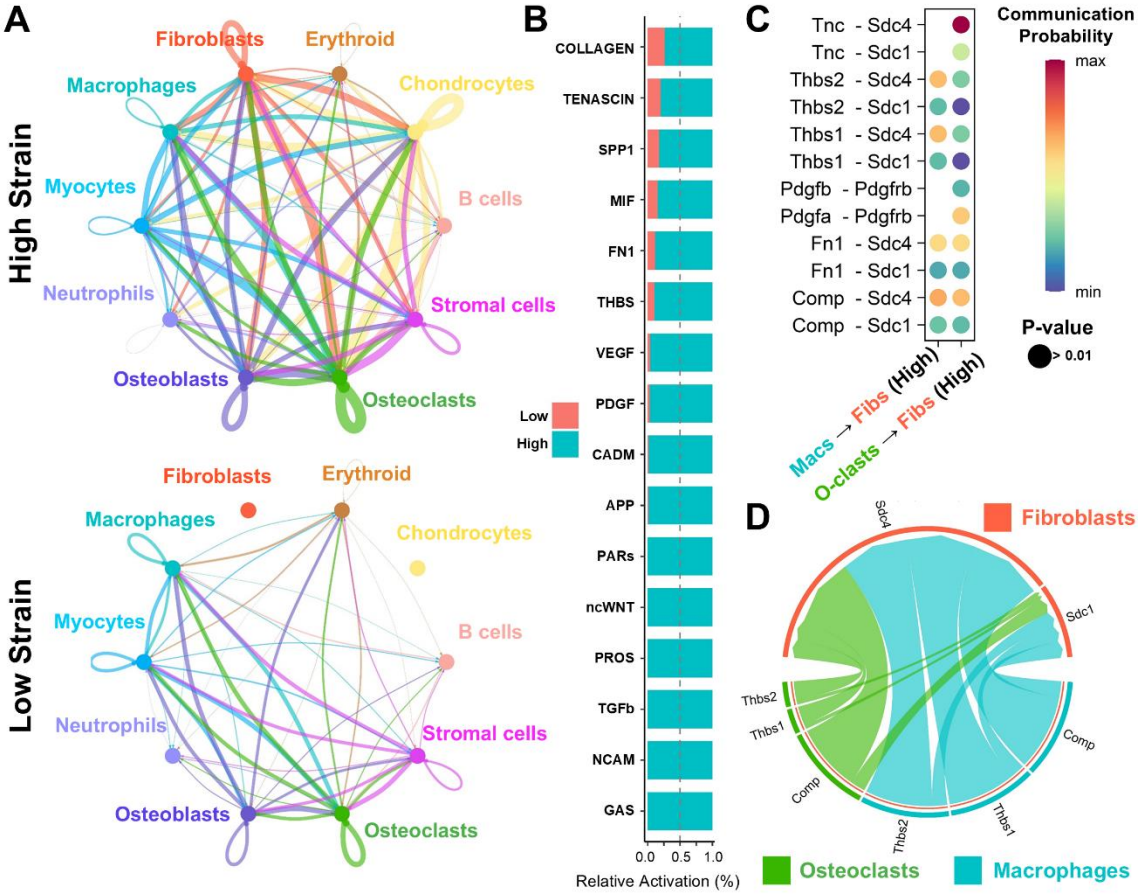

Figure 7. Mechano-Sensitive Cellular Networks Sustain Fibrotic Crosstalk. (A) *CellChat interaction networks in high-strain (top) and low-strain (bottom) calluses. Line thickness denotes interaction strength.* ***(B)*** *Relative activation levels of key signaling pathways, with most pathways showing increased activity in the high-*

strain calluses. ***(C)*** *Communication probability scores for key ligand-receptor interactions, with higher probability indicated by warmer colors.* ***(D)*** *Chord diagram highlighting major signaling interactions in high-strain calluses, with fibroblasts (red), macrophages (green), and osteoclasts (blue) as key mediators.*

4. Mechanical Instability Compromises Functional Healing Outcomes

Functional assessment via three-point bending at 3 weeks post-fracture revealed profound mechanical deficiencies in high-strain calluses (see **Table 4** for detailed values). Low-strain fractures exhibited superior whole-bone properties (**Fig.8A-D)**, with 1.6-fold higher stiffness (p = 0.024, **Fig. 8A**), 1.4-fold greater maximum force (p = 0.036, **Fig. 8B**), and 1.7-fold elevated ultimate stress (p = 0.002, **Fig. 8G**) compared to high-strain groups. The tissue-level properties (**Fig.8E-H**) further demonstrated impaired healing in high-strain calluses, with yield stress reduced by 1.9-fold (p = 0.032, **Fig. 8H**). While force-at-yield, post-yield displacement (PYD), work-to-fracture, and elastic modulus showed no significant differences (**Fig. 8C–F**), elastic modulus strongly correlated with callus volume (R = 0.87, p < 0.0001), underscoring that aberrant callus expansion in high-strain groups fails to restore structural integrity.

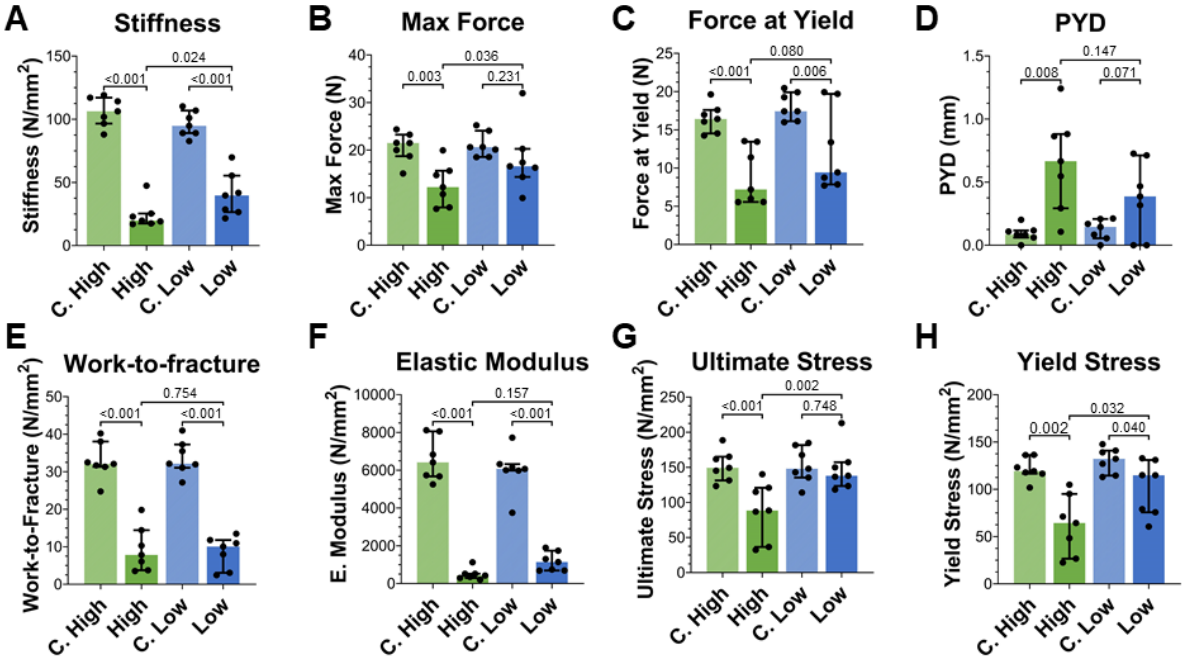

Figure 8. Interfragmentary Strain Determines Biomechanical Outcomes of Fracture Healing. *Three-point bending analysis of femurs at 3 weeks post-fracture.* ***(A–D)*** *Whole-bone properties: stiffness (A), maximum force (B), force at yield (C), and post-yield displacement (PYD, D).* ***(E–H)*** *Tissue-level properties: work-to-fracture (E), elastic modulus (F), ultimate stress (G), and yield stress (H). Low-strain groups (5% interfragmentary strain) significantly outperformed high-strain groups (15% strain) in stiffness (p = 0.024), maximum force (p = 0.036), ultimate stress (p = 0.002), and yield stress (p = 0.032). Data are median ± interquartile range; n = 12 per group. Contralateral controls (C. High, C. Low) represent uninjured femurs.*

5. Interfragmentary strain influences the systemic immune response.

Longitudinal profiling of peripheral immune cells revealed that interfragmentary strain dynamically modulates local and systemic inflammation. Within one hour post-fracture, a rapid decline

in circulating B cells and monocytes/macrophages occurred in both high- and low-strain groups (**Fig. 9A–B**), reflecting early recruitment of these cells to the injury site. However, by day 1, stark divergences emerged: the low-strain group exhibited a 9.4% reduction in B cells (p = 0.001, Fig. **9A(ii)**) but a 6.8% increase in total CD3+ T cells (p = 0.004, **Fig. 9A(iii)**) compared to high-strain controls. CD4+ T helper cells, initially reduced in low-strain mice at 1 hour (2.8% decrease, p = 0.032), rebounded by day 1 (3% increase, p = 0.025, Fig. 9A(iv)), suggesting accelerated adaptive immune priming in mechanically stable fractures.

By contrast, high-strain fractures showed prolonged innate immune dominance, with no significant changes in cytotoxic T cells or Tregs (**Fig. 9A(v–vi)**) and stable neutrophil/monocyte populations (**Fig. 9B(ii–iii)**). By week 3, low-strain calluses harbored 14.3% more myeloid cells than high-strain calluses (52.9 ± 12.12% vs. 38.57 ± 11.55%, p = 0.043), though subtype distributions were similar. These findings underscore that mechanical instability delays the transition from innate to adaptive immunity, perpetuating a pro-inflammatory state that correlates with poor healing outcomes.

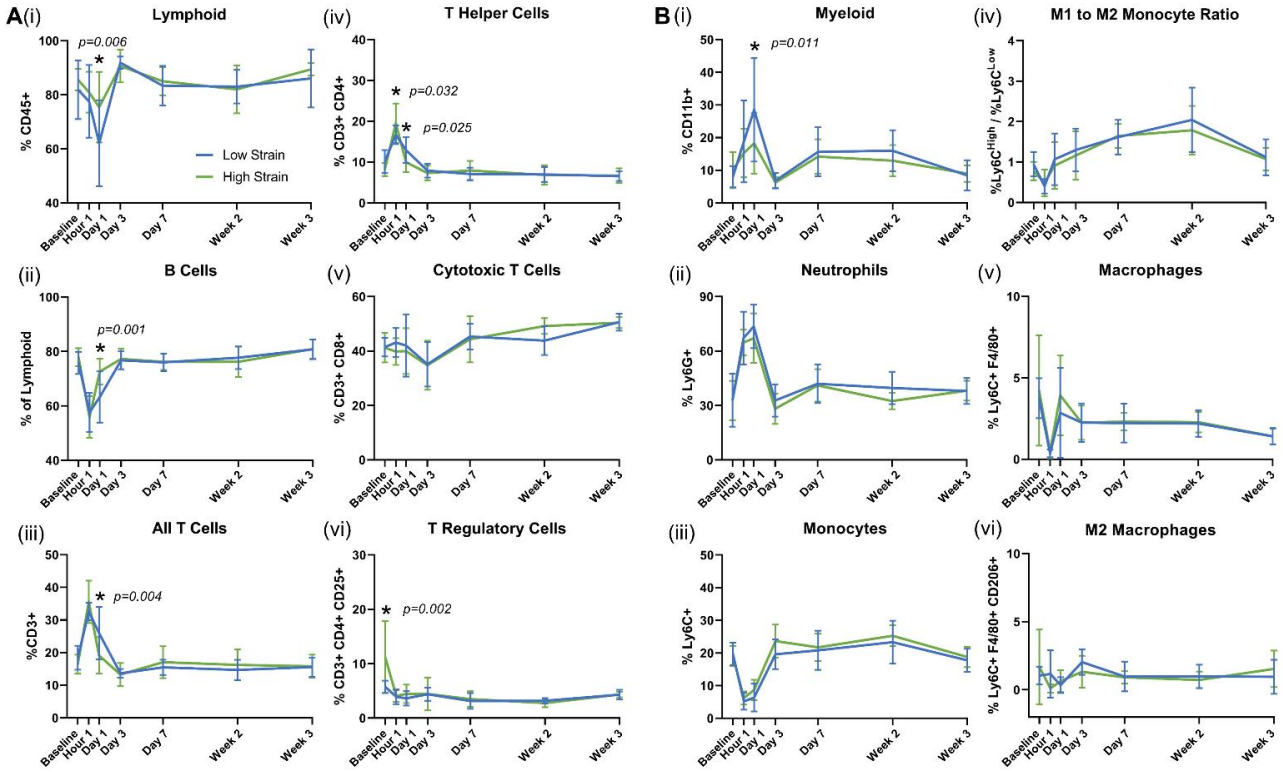

Figure 9. Interfragmentary Strain Dictates Temporal Immune Polarization Post-Fracture. *(**A**) Lymphoid cell dynamics: (**i**) Total CD45+ lymphoid cells, (**ii**) B cells, (**iii**) CD3+ T cells, (**iv**) CD4+ T helper cells, (**v**) CD8+ cytotoxic T cells, and (**vi**) CD25+ Tregs in peripheral blood.* ***(B)*** *Myeloid cell dynamics: (**i**) Total CD11+ myeloid cells, (**ii**) Ly6G+ neutrophils, (**iii**) Ly6C+ classical monocytes, (**iv**) M1 to M2 monocyte ratio, (**v**) F4/80+ macrophages, and (**vi**) CE206+ M2 macrophages. Low-strain groups (5% interfragmentary strain) exhibit early CD4+ T cell expansion and B cell contraction, while high-strain groups (15% strain) maintain innate dominance. Data are mean ± SEM; n = 7 per group; Baseline values were captured 5 days before fracture.*

6. Systemic and Local Immune Signatures Predict Biomechanical Healing Outcomes

Linear regression analysis identified 36 immune factors, spanning cell populations, cytokines, and chemokines, that correlated with functional healing outcomes (**Table 5**). Strikingly, MIP-1α levels at day 7 post-fracture showed robust positive correlations with elastic modulus (R = 0.970, p = 0.0013) and stiffness (R = 0.917, p = 0.009), while LIF (leukemia inhibitory factor) at day 3 correlated strongly with stiffness (R = 0.986, p = 0.014) and elastic modulus (R = 0.970, p = 0.030), underscoring their roles as early prognostic biomarkers.

Neutrophil population at day 7 correlated with maximum force (R = 0.59, p = 0.027) and ultimate stress (R = 0.59, p = 0.028), while day 21 callus monocytes exhibited divergent associations: M1 monocytes negatively correlated with ultimate stress (R = -0.56, p = 0.037), whereas M2 monocytes showed a positive correlation (R = 0.59, p = 0.037). CD4+ T cells in day 21 callus inversely correlated with stiffness (R = -0.57, p = 0.034), suggesting localized immune regulation impacts structural integrity.

Temporal shifts in T cell phenotypes further highlighted immune-healing dynamics (**Fig. 10**). At day 1, total CD3+ T cells positively correlated with ultimate stress (R = 0.71, p = 0.005, **Fig. 10A(i)**), while CD25+ Tregs showed a negative association (R = -0.59, p = 0.026, **Fig. 10A(ii)**). By day 14, CD8+ cytotoxic T cells negatively correlated with ultimate stress (R = -0.62, p = 0.017, **Fig. 10B(i)**), whereas Tregs exhibited a positive correlation (R = 0.58, p = 0.030, **Fig. 10B(ii)**). These findings underscore that early pro-regenerative immune polarization, driven by Tregs and M2 monocytes, supports functional repair, while prolonged inflammation (M1 monocytes, CD8+ T cells) impedes healing.

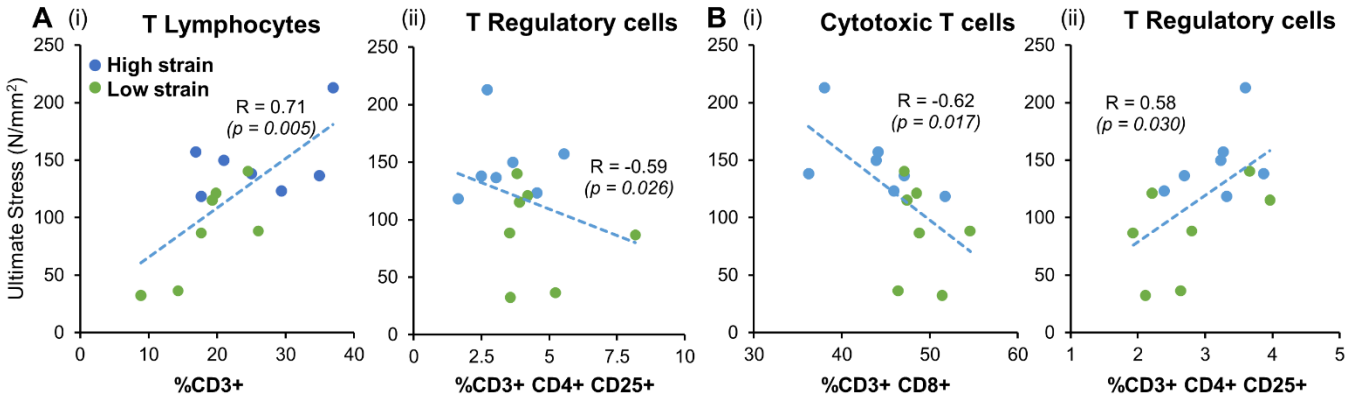

Figure 10. Temporal Immune Polarization Predicts Biomechanical Healing Outcomes. *(**A**) Day 1 post-fracture: (**i**) Positive correlation between CD3+ T cell frequency and ultimate stress (R = 0.71, p = 0.005). (**ii**) Negative correlation between CD25+ Treg frequency and ultimate stress (R = -0.59, p = 0.026). (**B**) Day 14 post-fracture: (**i**) Negative correlation between CD8+ T cell frequency and ultimate stress (R = -0.62, p = 0.017). (**ii**) Positive correlation between CD25+ Treg frequency and ultimate stress (R = 0.58, p = 0.030). Data are linear regression fits with 95% confidence intervals, n = 12 per group.*

7. Identification of immune phenotypes as predictors of functional healing

To identify immune biomarkers predictive of fracture healing, we applied partial least squares regression (PLSR) to integrate longitudinal immune profiles (1 hour to 21 days post-fracture) with biomechanical outcomes. PLSR revealed distinct immune trajectories separating high- and low-strain groups, with maximal predictive power at 1 hour (R = 0.71, p = 0.005), day 3 (R = 0.57, p = 0.032), and day 14 (R = 0.72, p = 0.004) post-fracture (**Fig. 11**). CD206+ macrophages at 1 hour (weighted coefficient = 0.228) and F4/80+ macrophages at day 3 (weighted coefficient = 0.206) emerged as dominant early

predictors of healing. By day 14, CD25+ regulatory T cells (Tregs) (weighted coefficient = 0.958) and CD206+ macrophages (weighted coefficient = 0.233) were the strongest predictors of day 21 biomechanical outcomes, highlighting the transition from innate to adaptive immune regulation as a critical determinant of repair.

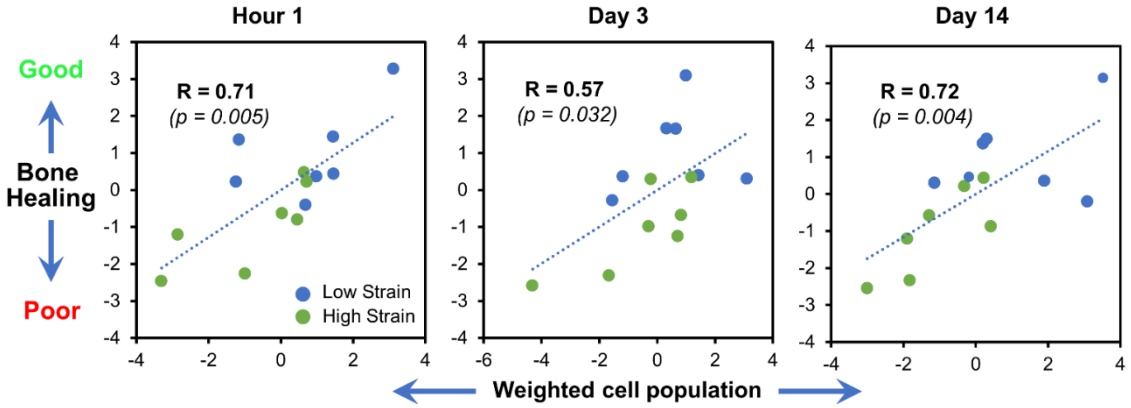

Figure 11. Early Immune Profiles Predict Biomechanical Outcomes of Fracture Healing. *Partial least squares regression (PLSR) analysis of systemic immune cell populations (X matrix) against functional healing outcomes (Y matrix: stiffness, maximum force, ultimate stress, elastic modulus). PLSR score plot demonstrates maximal separation between high- (15% strain) and low-strain (5% strain) groups at 1 hour, day 3, and day 14 post-fracture. Weighted coefficient values in the model identify CD206+ macrophages (1 hour, day 14) and CD25+ Tregs (day 14) as top predictors. Data are mean ± 95% confidence intervals; n = 12 per group.*

C. Discussion

1. A Clinically Relevant Murine Model of Strain-Driven Hypertrophic Nonunion

Hypertrophic nonunion, driven by mechanical instability, remains a major clinical challenge due to delayed diagnosis and a lack of non-surgical therapies. Existing animal models, which focus on biologically deficient atrophic nonunion or prolonged segmental defects, fail to replicate the mechanopathology of clinical hypertrophic nonunion[21]. To address this, we developed a murine model using tunable nitinol intramedullary nails to impose controlled interfragmentary strains (High:15-30% vs. Low:<5%), mirroring the mechanical instability central to human hypertrophic nonunion. This system enables precise investigation of strain-dependent mechanisms driving impaired healing.

Interfragmentary strain is the primary mechanical determinant of fracture stability, governing inflammation, vascularization, osteogenesis, and osteoclastogenesis[22]. Excessive strain disrupts these processes, leading to fibrosis and nonunion[23]. Leveraging nitinol, a superelastic alloy with optimal mechanobiological properties[24,25], we engineered IM nails of varying stiffness to establish two distinct mechanical environments. Low-stiffness nails permitted high strain (15–30%), while high-stiffness nails restricted strain to <5%, stabilizing fractures akin to clinical best practices.

High-strain fractures (>15%) formed larger calluses with 1.7-fold greater tissue volume but exhibited impaired ossification and biomechanical integrity compared to low-strain controls. This paradoxical callus expansion without functional healing aligns with clinical observations where excessive strain disrupts the transition from fibrotic tissue to mineralized bone[26]. Unlike segmental defect models where callus volume correlates with healing[27,28], our model demonstrates that high strain, even

with bone fragments in close proximity, creates a maladaptive microenvironment favoring fibrosis. Critically, callus bone volume fraction (BV/TV) and mineral density (BMD) remained comparable between groups, confirming that mechanical instability, not biological deficiency, drives impaired healing. By recapitulating the strain-dependent etiology of human hypertrophic nonunion, this model provides a platform to dissect mechano-immunological pathways and test therapeutic strategies under clinically relevant conditions.

2. Mechano-Immunological Drivers of Fibrotic Remodeling

The magnitude and direction of interfragmentary strain and shear forces play a crucial role in secondary fracture healing[29]. Mechanical instability induces translational shear forces that exacerbate fibrosis by dysregulating immune-stromal crosstalk[30-32]. Spatial transcriptomics revealed fibroblast-rich niches in high-strain calluses (14-fold increase vs. low-strain) co-localized with *Lgals3*+ macrophages and *Mmp9*+ osteoclasts (**Fig. 5B–C**). Macrophages in these niches overexpressed *Spp1* (osteopontin), *Pdgfrb*, and *Lgals3* (galectin-3), genes linked to fibroblast activation and sustained fibrosis. Notably, *Lgals3*+ macrophages, known drivers of chronic fibrosis in muscular dystrophy[33], spatially aligned with fibroblasts, suggesting direct cell-cell crosstalk (**Fig. 6B**).

This interaction was potentially mediated by the THBS-SDC4 signaling axis, where macrophages secreted thrombospondin-1/2 (*Thbs1/2*) to engage fibroblast syndecan-4 (*Sdc4*) receptors[34]. *SDC4*, a regulator of cell adhesion and focal adhesion assembly, stabilized fibroblast-macrophage interactions, promoting adhesion-dependent fibrotic remodeling (**Fig. 7D**). Concurrently, *Mmp9*+ osteoclasts in high-strain calluses exacerbated fibrosis by activating latent TGF-β through collagen degradation, further amplifying fibroblast proliferation and ECM dysregulation[35,36].

Gene Ontology (GO) enrichment analysis confirmed significant upregulation of pathways tied to fibroblast regulation (e.g., *PDGF* signaling) and ECM organization (e.g., collagen fibril assembly), with macrophages as primary contributors (**Fig. 6E**). Osteoclasts and osteoblasts exhibited complementary roles in ECM disassembly and ossification, respectively (**Tables 2–3**), highlighting their dual function in strain-dependent matrix remodeling. Together, these mechanisms create a self-reinforcing fibrotic loop, where mechanical instability sustains maladaptive immune-stromal crosstalk, ultimately impairing functional bone healing.

3. Immune dysfunction and biomarkers to predict functional healing.

Understanding the dynamic interplay between immune responses and bone regeneration is critical for identifying therapeutic targets and prognostic biomarkers. While the traditional phases of fracture healing, inflammation, soft callus formation, hard callus formation, and remodeling, are well-described, the role of systemic immune dysregulation in delayed healing remains poorly defined. Prior work by Reinke and colleagues demonstrated that elevated levels of terminally differentiated $CD8^+$ TEMRA cells in peripheral blood correlated with delayed healing in human fractures, where these cells infiltrated fracture hematomas and inhibited osteogenesis through IFN-γ and TNF-α secretion, impairing mesenchymal stromal cell function[37] Similarly, our study found that high-strain fractures exhibited persistent $CD8^+$ T cells and reduced $CD25^+$ Tregs, recapitulating the immune signatures of unresolved inflammation that Reinke et al. identified as prognostic of poor outcomes. This connection

underscores the translational relevance of our murine model in capturing immune patterns predictive of delayed healing in patients.

Complementing this, Hebb et al. used transcriptomic profiling of aged murine fractures to show that aging correlates with sustained inflammation and delayed osteogenic gene expression, particularly an enrichment of $CD8^+$ cells and macrophages in aged calluses[38]. Their findings parallel our observations in mechanically unstable environments, where persistent inflammation and altered macrophage polarization correlated with fibrotic remodeling and impaired healing. Together, these studies point to a convergent mechanism by which chronic inflammation, whether strain-induced or age-associated, creates an immune milieu unfavorable to regeneration.

To further investigate this relationship, we conducted comprehensive immune profiling across stable (low-strain) and unstable (high-strain) fractures. Early-phase healing (1 hour–7 days post-fracture) was marked by pro-healing myeloid recruitment (MIP-1α, IL-1α[39]) and osteogenic cytokine release (LIF[40]). In contrast, delayed healing in high-strain groups correlated with persistent CD8+ T cells and M1 monocytes, alongside reduced CD25+ Tregs, a signature of unresolved inflammation. These findings align with clinical reports of dysregulated leukocyte kinetics in nonunion patients[41], emphasizing the importance of timely immune transition from proinflammatory debris clearance to pro-regenerative osteoblast activity[42].

Next, we performed an in-depth analysis of cell populations using multivariate PLSR algorithm to predict functional bone healing. PLSR identified CD206+ macrophages (1-hour post-fracture) and CD25+ Tregs (day 14) as dominant prognostic biomarkers. CD206+ macrophages facilitated early inflammation resolution, while Tregs suppressed chronic immune activation, enabling osteoblast-driven repair. This mechanistic insight underscores the potential of immune profiling for early diagnosis and therapeutic targeting.

4. Limitations and Clinical Translation

While our model recapitulates the mechanopathology of clinical hypertrophic nonunion, several limitations must be acknowledged. First, murine fractures inherently heal within 6–9 weeks, meaning our model reflects 'delayed healing' rather than permanent nonunion. This distinction is critical, as human nonunions often require surgical intervention and do not resolve spontaneously. However, this model captures the early pathogenic window where mechanical instability drives fibrosis and immune dysregulation, offering insights into mechanisms that may precede chronic nonunion in humans. Second, the inability to continuously monitor interfragmentary strain *in vivo* limited our ability to correlate dynamic mechanical changes with immune responses in real time. However, our findings align with *in silico* models predicting that elevated strain leads to fibrosis and nonunion[28]. Future integration of strain-sensing technologies could refine this relationship. Third, while we identified key fibrotic (*THBS-SDC4*, *Lgals3*) and immune (CD206+ macrophages, Tregs) mediators, the pleiotropic nature of immune cells and cytokines suggests additional pathways may contribute to delayed healing. Broader profiling of cytokine networks could uncover novel targets. Finally, interspecies differences in immune responses and healing capacity necessitate validation in larger preclinical models to assess translational relevance.

D. Summary and Conclusion

We developed a murine delayed-healing model that faithfully replicates the early etiology of hypertrophic nonunion by coupling mechanical instability with maladaptive immune-fibrotic crosstalk. Although all murine fractures ultimately heal, this model isolates the critical period where excessive strain disrupts regeneration, providing a platform to study mechanisms that may precede chronic nonunion in humans. Our findings redefine hypertrophic nonunion as a disorder of mechano-immunology, driven by *Thbs1-Sdc4* signaling and *Lgals3+* macrophage-mediated fibrosis, and identify CD206+ macrophages and Tregs as early prognostic biomarkers. By bridging biomechanics and immunology, this work lays the groundwork for mechano-informed therapies for the early detection and prevention of delayed healing as well as the prevention and treatment of nonunions, addressing a major unmet need in orthopedic trauma care.

E. METHODS

1. Animal model and surgical procedures

All animal procedures adhered to the guidelines approved by the Institutional Animal Care and Use Committee (IACUC) at the University of Kentucky. Adult male C57BL/6 mice (22-24 weeks old, The Jackson Laboratory) were used in this study. Prior to any procedures, animals underwent a minimum 7-day acclimatization period. The mice were randomly allocated into two experimental groups, comprising low and high-stiffness intermediary nails (n = 12/group). The intermediary nails were custom-manufactured from nitinol rods (Chamfr), with diameters ranging from 0.31 to 0.51 mm to modulate stiffness.

An established transverse fracture model[19]was employed to create femoral fractures. This method does not require any incisions of the muscles and mimics the fracture resulting from blunt trauma in humans with reproducible precision[43,44]. Briefly, mice were anesthetized (1.5 mg of ketamine/kg + 1.5 mg of xylazine/kg body mass of mice), a bland ophthalmic ointment was applied, and the surgical site was shaved and wiped with 70% ethanol, followed by 10% povidone-iodine solution. A small incision was made at the patella and laterally dislocated to expose the knee joint. Using a 0.5 mm centering bit, a hole was made in the intercondylar notch, and an intramedullary guide tube (NiTi, 0.2 mm diameter) was inserted into the femur. With the guide tube in place, the right leg was positioned under the guillotine (blunt striker) of the murine fracture apparatus (RISystems). The blunt striker was then released to produce impact kinetic energy (E_k) of ~40 mJ, which is shown to create a transverse fracture in adult C57BL/6 mice[45]. The guide tube was then replaced with appropriate intermediary nails to stabilize the femur. The skin at the patella was sutured with 6-0 vicryl suture (Ethicon). Then, 1 mL of saline was administered intraperitoneally for hydration, followed by subcutaneous administration of buprenorphine SR (1.5 mg/kg body mass) for analgesia. The animals were then placed into a recovery cage and monitored as per the established post-operative animal care protocols. Animals were monitored daily for 7 days and weekly thereafter to ensure post-operative recovery.

2. Tissue collection and processing

Blood samples were also collected longitudinally from mice in K2 EDTA Microvette tubes (Sarstedt) from the submental and submandibular veins, following an alternating schedule. Baseline samples were obtained five days prior to surgery, with subsequent samples taken at 1 hour, 1, 3-, 7-, 14-, and 21-days post-surgery. Blood samples were centrifuged at 900 g for 5 minutes to separate cells from plasma. The supernatant containing plasma was stored at -80°C until analyzed using a multiplex assay kit. The cellular fraction of the blood was then processed, stained, and analyzed using flow cytometry.

For analyzing callus tissue cell populations, callus tissue at day 21 was minced, digested in a 0.1% collagenase solution (MP Millitec) at 37°C for 2 hours, neutralized with Dulbecco's modified Eagle's media (DMEM, Gibco) containing 10% fetal bovine serum (FBS, Gibco), filtered through a 100 μm cell strainer, and centrifuged at 400 g for 5 minutes to remove the supernatant. The cell pellet was then processed, stained, and analyzed using flow cytometry.

At 21 days post-surgery, the animals were euthanized, and their femurs (fractured and contralateral control) were collected in Dulbecco's modified Eagle's media (DMEM). The bones were

subjected to morphometric analysis and biomechanical testing at room temperature. For histological analyses, the samples were then fixed in 10% neutral buffered formalin (ThermoFisher Scientific) for 24 hours, stored in 10 mM PBS at 4°C, and analyzed as described below.

3. MicroCT and morphometric analysis

Fracture healing outcomes were assessed at week 3 post-surgery using microcomputed tomography (microCT), as described[46]. To prevent any interference from the intramedullary nails, they were meticulously removed before the scanning process. A 360° scan was performed using a high-resolution small animal imaging system SkyScan1276 microCT (Bruker, Billerica, MA) with a 1 mm Aluminium filter with the voltage set to 70 kV and image pixel size 20.32 μm. Images were then reconstructed (NRecon, Bruker) with smoothing (set to 3), ring artifact correction (set to 4), and beam hardening correction (set to 30%). In preparation for morphometric analysis, cylindrical phantoms with diameters of 2 mm and known bone mineral densities of 0.25 and 0.75 g/cm^3 were submerged in deionized water, scanned, and reconstructed using the same settings.

The cortical region of the bone was delineated using a five-level Otsu algorithm. The threshold values for each level were determined based on the contralateral femur. Level 3 was scrutinized against the raw grey scale images to ensure the accuracy of the threshold, and it was subsequently employed as the cutoff threshold for analyzing the cortical region of the fractured bone. A 5 mm section (± 2.5 mm from the fracture) at the fracture site was designated as the Volume of Interest (VOI), with the cortical bone being defined as the Region of Interest (ROI). The ROI was processed algorithmically within the CTan software by Bruker to ensure consistent and precise analysis of both the callus and cortical bone separately. An adaptive threshold (Mean-C) was applied to the callus region to accommodate variations in mineral density and ensure alignment with the raw grey scale images. Three-dimensional analyses were then carried out on the callus and cortical sections using these chosen thresholds. The CTvox software (Bruker) was utilized to construct three-dimensional volume-rendered images of the bone.

4. Mechanical testing

Biomechanical properties of the bone were evaluated via a three-point bending test, as described previously[47]. The fracture and contralateral femurs were weighed, and their dimensions were determined through digital analysis of microCT scans. The three-point bending tests were executed using a Universal Testing Machine (Instron) at a strain rate of 30 mm/min, with an 8 mm span length, all performed at room temperature. Comprehensive whole bone properties, encompassing parameters like stiffness, maximum force, work-to-fracture, and post-yield displacement (PDY), were deduced from the stress-strain curve. Furthermore, tissue-level parameters such as elastic modulus, yield stress, and ultimate stress were computed employing beam theory equations as listed below.

$$E = \frac{KL^3}{48I}$$

$$s_u = \frac{F_u Lc}{4I}$$

$$s_y = \frac{F_y Lc}{4I}$$

Where E = elastic modulus, K = stiffness, L = span length, I = moment of inertia, s_u = ultimate stress, F_u = ultimate force, c = distance from centroid of cross-section to outer most point on the cross-section, s_y = yield stress, and F_y = yield force. To calculate the average area moment of inertia (MOI) essential for these equations, a 5 mm segment (within ± 2.5 mm from the fracture site) was chosen from the microCT scans as the Volume of Interest (VOI), and a two-dimensional analysis was carried out.

The stiffness of the nitinol intramedullary nails was also measured through a 3-point bend test performed at a strain rate of 10 mm/min with an 8 mm span length. Stiffness was calculated from the slope of the linear region. The flexure strain of the stabilized femur was utilized as a metric for measuring the interfragmentary movement. It was computed under physiological loading conditions by employing the standard three-point flexure testing. The calculation for flexure strain in cylindrical geometries was as follows:

$$Flexture\ Strain = \frac{6Dd}{L^2}$$

Where D = axial displacement, d = cylinder diameter, and L = span length.

5. Histology

For histological examination, mice were euthanized on day 21 post-surgery. Subsequently, the femurs with fractures were meticulously dissected and stripped of adjacent muscle tissues. The collected femurs then underwent decalcification using a solution containing 10% EDTA 4Na $2H_20$ (Sigma ED4SS) and 9% EDTA 2Na $2H_20$ (Sigma E5134) in sterilized deionized water. For samples designated for Visium spatial transcriptomics 0.1% diethyl pyrocarbonate (Sigma D5758) was added to the decalcification solution to neutralize RNase enzymes. This decalcification solution was changed every three days over the course of three weeks. Following successful decalcification, the samples were paraffin-embedded and sectioned into 5 μm thick slices, which were subsequently mounted onto microscope slides (Apex Bond, Leica). The prepared slides were then subjected to staining using either a Movat's Pentachrome kit (StatLab) or a Picro-Sirius Red staining kit (StatLab), following the respective manufacturer's instructions or immunohistochemistry (IHC) as described previously.

Briefly, IHC was performed using the Ventana Discovery Ultra platform. 5 μm thick sections of formalin-fixed paraffin-embedded (FFPE) tissue were deparaffinized onboard, followed by on-board antigen retrieval as detailed below, primary antibody incubation at 37°C for 1 hour, detection as indicated below, and visualization with Ventana ChromoMap DAB.

SOX9 (Cell signaling 82630 at 1:200) and SP7 (Thermo PA5-115697 at 1:100) were retrieved using Ventana CC1 buffer under standard conditions. Primary antibody was amplified by incubation with Ventana anti-rabbit-HQ, then anti-HQ-HRP for 20 minutes each. CD-31 (cell signaling 77699 at 1:100) was retrieved using Ventana CC2 standard with primary amplification and detection as above. SMA (Abcam ab5694 at 1:500) used CC1 standard and detection of primary antibody by Ventana OmniMap anti-rabbit-HRP. All slides were run concurrently with known positive control tissue to confirm assay performance.

Immunohistochemical quantification was conducted using QuPath (v0.5.1). For each sample, 3–5 regions of interest (500 × 500 pixels) were manually placed within either the intramedullary or

periosteal callus compartments, with selection prioritized along the fracture line within a ±2 mm margin. Positive cell percentages were calculated within each region and averaged per sample to account for tissue heterogeneity. Group-level means were then derived from 3–4 representative slides per condition, excluding any slides exhibiting significant tissue detachment. Stained slides were then imaged on an Axioscan Z7 with pentachrome and IHC-stained slides being imaged under bright field light and Picro-Sirius Red slides being imaged under both bright field and polarized light. The fibrotic area was measured using Zeiss image analysis software. Only slides including the center section of the femur and fracture callus were used for analysis. The fibrotic tissue areas were manually selected with the area calculation tool and summed together to get the total fibrotic area per slide. Fibrotic areas were defined by the presence of fibrillar collagen visible under polarized light. Fibrotic areas were only measured if they were inside the fracture callus or within the fracture gap in the medullary canal.

6. Spatial Transcriptomics

We prepared libraries for 10X Genomics Visium CytAssist following the manufacturer's guidelines. Formalin-fixed paraffin-embedded (FFPE) tissue sections (5 μm thick) were positioned on charged glass slides and baked at 42°C for three hours. After deparaffinization and Hematoxylin and Eosin (H&E) staining, high-resolution imaging was performed using a Leica Aperio AT2. Decrosslinking was carried out, followed by an overnight probe hybridization. Both left-hand and right-hand probes were ligated, and tissues were stained with Eosin. The slide, equipped with the appropriate CytAssist Gene Expression slide, probe release, and tissue digestion master mix, was inserted into the CytAssist. A low-resolution image was captured by the CytAssist for fiducial frame alignment, and probes were transferred from the charged glass slide and tissue onto the Gene Expression slide. The probes underwent elongation and subsequent elution from the Gene Expression slide, followed by amplification and purification. The final index PCR cycles were determined via qPCR (Kapa; Agilent). The quality of the final library was evaluated using the LabChip GX Touch HT (Revvity), and libraries were quantified using Qubit. Pooled libraries were then subjected to paired-end sequencing as per the manufacturer's protocol (Illumina NovaSeqXPlus). BclConvert software (Illumina) was employed to generate de-multiplexed Fastq files. The CytAssist and high-resolution images were aligned using the 10X Genomics Loupe Alignment software, and the SpaceRanger Pipeline (10X Genomics) was utilized to align reads and generate count matrices. This enabled us to evaluate the differential expression between spots at a resolution of 55 μm.

LoupeR was used to carefully manually select the desired region of interest within the samples, mainly focusing on callus and intramedullary canal 1-2 mm surrounding the fracture line. We processed count matrices from sequencing data using R (version 4.3.2). Quality assessment involved filtering out cells with low unique molecular identifiers (UMI) or gene expression. Analysis regions with < 500 UMIs or < 250 expressed genes were excluded. Additionally, genes not expressed in at least three Analysis regions were removed. We evaluated the impact of mitochondrial expression and cell cycle effects and adjusted for them as needed. The Seurat (version 4.4.0)[48] package was employed for post-processing, including normalization (SCTransform v2), integration, principal component analysis (PCA), uniform manifold approximation and projection (UMAP), and clustering (40 dimensions, clustering resolution of 1.4). Clusters were assigned to cell types using ScType[49] and a custom gene set for bone cells derived

from the Panglao database[50]. Manual validation based on highly expressed unique genes confirmed cell type assignments. Differential gene expression analysis of cell types between test groups (high and low strain groups) utilized the Wilcoxon rank sum test with Bonferroni correction. Differentially expressed genes (DEGs) were filtered to only include genes with an average log_2 fold change of > 0.25 or < -0.25 and adjusted p value < 0.05. The filtered up and down- regulated genes were then analyzed through gene ontology (GO) enrichment of biological processes using clusterProfiler (version 4.8.3), AnnotationDbi (version 1.62.2), and org.Mm.eg.db (version 3.17.0) packages. Finally, communication networks between cell types were explored using the CellChat[51] package (version 2.1.2).

7. Flow cytometry and multiplex assay

Blood samples were collected at specific time points and processed as described above. Briefly, plasma was separated through centrifugation, and red blood cells (RBC) were lysed from the remaining sample following the manufacturer's guidelines using 1X RBC lysis buffer (eBioscience). Subsequently, an equal volume of 1X PBS (Gibco) was added to the suspension, followed by centrifugation at 400 g for 5 minutes. The resulting cell pellet was suspended in a blocking solution consisting of FACS buffer (1X PBS with 5% fetal bovine serum (Gibco) and 0.1% sodium azide) along with anti-mouse CD16/32 (eBioscience) for 10 minutes at 4°C to block Fc receptors.

The cells were then stained with fluorescently conjugated anti-mouse antibodies in FACS buffer for 45 minutes in the dark at 4°C. The detailed information regarding the fluorescent conjugates, clones, dilution factors, and suppliers for these antibodies can be found in **Supplementary Table 1**. The cell identification markers are listed in **Supplementary Table 2.** Following the staining procedure, the solution was removed through centrifugation at 400 g for 5 minutes, and the cells were subsequently resuspended in fresh FACS buffer. The samples were promptly subjected to analysis using a BD FACSymphony A3, and the data were processed using FlowJo software. Fluorescence-minus-one (FMO) controls for each antibody were employed to establish negative gates, ensuring a noise level of less than 1%.

To investigate the presence of inflammatory proteins, cytokines, and chemokines in the blood samples, a 32-analyte Milliplex MAP Mouse Cytokine/Chemokine Panel (Millipore, MCYTMAG-70K-PX32) was utilized. Initially, the plasma was isolated as previously described and then diluted in accordance with the manufacturer's recommendations.

8. Univariate and multivariate analysis

We conducted a comprehensive multifaceted analysis to investigate the relationship between immune cell populations, biochemical factors in both blood and callus tissues, and healing outcomes through conventional linear regression. Additionally, we employed multivariate models including linear and logistic regression. This included partial least squares regression (PLSR) analysis, which incorporated weighted averages of cell populations, cytokines, chemokines, and healing outcomes to identify the most influential immune factors. We utilized predictive analytics software JMP-PRO for all analyses. PLSR created principal components (latent variables, LV) combining immune cells, factors, and healing measures, and we assessed their predictive power by correlating them with the immune factors. We considered quadratic terms and variable interactions to enhance the model fits and employed the

NIPALS algorithm with a 7 KFOLD validation method for generating linear plots. Notably, we focused on the first two linear combinations to identify the most influential healing factors.

9. Statistics

Data are plotted as either means with error bars representing the standard deviation or median with error bars representing the interquartile range. The Pearson correlation coefficient (r) was used to evaluate the linear correlation between two variables, and the t-distribution was used to evaluate the associated p-value. To ensure the reliability of statistical comparisons, we subjected all groups to tests for normality and equal variance, employing the Shapiro-Wilk and Brown-Forsythe tests, respectively. In cases where both conditions were met, we used Student's T-test for two independent groups. When normality was not met, we applied the Mann-Whitney Rank Sum Test, and if the equal variance test failed, a Welch's t-test was used. For the analysis of systemic markers over time, a 2-way repeated measures ANOVA was performed. All statistical tests were performed in JMP or GraphPad Prism. Differences with $p < 0.05$ were considered statistically significant.

ACKNOWLEDGEMENTS

Research reported in this publication was supported in part by the National Institute of Arthritis and Musculoskeletal and Skin Diseases (NIAMS) Award Numbers R21AR078447 and R01AR066028, National Institute of General Medical Sciences (NIGMS) of the National Institutes of Health under Award Number P20GM130456, Orthopedic Trauma Association (OTA, Grant Number: 6889), and Biospecimen Procurement & Translational Pathology Shared Resource Facility of the University of Kentucky Markey Cancer Center Award Number P30CA177558. Library prep and next-generation sequencing were carried out in the Advanced Genomics Core at the University of Michigan. We gratefully acknowledge the late Dr. Arnold Stromberg (Department of Statistics, University of Kentucky) for his invaluable contributions to statistical modeling and analysis.

The content is solely the responsibility of the authors and does not necessarily represent the official views of the National Institutes of Health or other grant funding agencies.

F. TABLES:

Table 1. Bone morphometric analysis.

The values presented are expressed as mean±SD. The sample size (n) for both groups is 12.

Morphometric properties	High Strain	Low Strain	p-value
Callus TV (mm^3)	44.72 ± 9.9	29.47 ± 11.1	0.0028
Callus BV (mm^3)	23.31 ± 5.6	14.45 ± 5.1	0.0009
Callus Mineral content (mg)	14.45 ± 3.8	7.95 ± 2.8	0.0002
Callus BV/TV (%)	52.08 ± 3.2	49.45 ± 5.1	0.1652
Callus BMD (mg/mm^3)	0.62 ± 0.1	0.55 ± 0.1	0.0536
Callus Trabecular Thickness (mm)	0.115 ± 0.003	0.117 ± 0.004	0.2391
Callus Trabecular Number (mm^{-1})	4.51 ± 0.3	4.23 ± 0.5	0.140
Callus Trabecular Separation (mm)	0.16 ± 0.04	0.16 ± 0.1	0.8180
Callus Bone Surface (mm^2)	618.89 ± 140.6	384.03 ± 129.1	0.0006
Callus Bone Surface Density (mm^2/mm^3)	13.85 ± 0.7	12.98 ± 1.4	0.0902
Callus Specific bone surface (mm^2/mm^3)	26.61 ± 0.9	26.78 ± 1.1	0.6916
Callus Structure Model Index (SMI)	-0.69 ± 0.3	-0.26 ± 0.5	0.0204
Callus Connectivity density (mm^{-3})	196.87 ± 23.1	167.57 ± 29.5	0.0174
Callus Degree of anisotropy	1.25 ± 0.1	1.43 ± 0.2	0.0054

Table 2. Spatial Transcriptomics Fibrotic Expression Analysis.

The values presented are log2 Fold changes.

S. No	Gene Symbol	High vs. Low (Log2 Fold change)	Adj. P value	Cell type expression rich area
1	*Comp*	1.159	<0.0001	Macrophages
2	*Mgp*	1.140	<0.0001	Macrophages
3	*Spp1*	0.933	<0.0001	Macrophages
4	*Ctsk*	0.839	<0.0001	Macrophages
5	*Pdgfrb*	0.754	<0.0001	Macrophages
6	*Rarg*	0.634	0.0007	Macrophages
7	*Lgals3*	0.583	0.0137	Macrophages
8	*Dmp1*	0.745	<0.0007	Osteoblasts
9	*Ctsk*	0.556	0.0016	Osteoblasts
10	*Acp5*	0.536	0.0001	Osteoblasts
11	*Fgfr1*	0.517	<0.0001	Osteoblasts

12	*Ctnnb1*	0.415	<0.0001	Osteoblasts
13	*Pdgfa*	0.388	0.0014	Osteoblasts
14	*Ctsk*	1.450	<0.0001	Osteoclasts
15	*Acp5*	1.433	<0.0001	Osteoclasts
16	*Mmp9*	1.026	<0.0001	Osteoclasts
17	*Dmp1*	0.994	<0.0001	Osteoclasts
18	*Mmp13*	0.852	<0.0001	Osteoclasts
19	*Spp1*	0.629	<0.0001	Osteoclasts
20	*Fgfr1*	0.558	0.0003	Osteoclasts
21	*Pdgfa*	0.499	0.0029	Osteoclasts
22	*Ctnnb1*	0.655	<0.0001	B cells
23	*Mmp9*	0.598	<0.0001	B cells
24	*Pdgfrb*	0.576	<0.0001	B cells
25	*Spp1*	0.432	0.0026	B cells

Table 3. Spatial Transcriptomics Collagen Expression Analysis.

The values presented are log2 Fold changes.

S. No	Gene Symbol	High vs. Low (Log2 Fold change)	Adj. P value	Cell type expression rich area
1	Col5a1	0.461	0.0404	Macrophages
2	Col5a1	0.796	<0.0001	Osteoblasts
3	Col2a1	0.655	<0.0001	Osteoblasts
4	Col13a1	0.595	<0.0001	Osteoblasts
5	Col5a2	0.532	<0.0001	Osteoblasts
6	Col4a2	0.461	<0.0001	Osteoblasts
7	Col11a2	0.387	<0.0001	Osteoblasts
8	Col16a1	0.337	0.0459	Osteoblasts
9	Col5a1	0.789	<0.0001	Osteoclasts
10	Col5a2	0.430	<0.0001	Osteoclasts
11	Col5a2	0.788	<0.0001	B cells
12	Col1a2	0.658	<0.0001	B cells
13	Col4a1	0.559	<0.0154	B cells
14	Col11a2	0.423	<0.0001	B cells

Table 4. Assessment of fracture healing outcomes.

Comparative evaluation of whole-bone and tissue-level mechanical properties of femurs subjected to 3-point bending testing. Values are presented as mean±SD. n = 7 for both groups.

	Control High strain	**High Strain**	**Control Low Strain**	**Low Strain**	**High vs Low p-value**	**C. High vs High p-value**	**C. Low vs Low p-value**
Stiffness (N/mm)	106.16 ± 11.5	24.17 ± 10.7	96.26 ± 10.2	40.48 ± 17.2	0.024*	<0.001*	<0.001*
Max load (N)	20.64 ± 3.1	12.72 ± 4.4	21.11 ± 2.6	18.19 ± 6.9	0.036*	0.003*	0.231
Force at Yield (N)	16.49 ± 1.8	8.95 ± 3.7	18.08 ± 1.8	12.39 ± 5.4	0.080	<0.001*	0.006*
Post-yield displace. (mm)	0.09 ± 0.1	0.66 ± 0.4	0.12 ± 0.1	0.38 ± 0.3	0.147	0.008*	0.071
Work-to-fracture (Nmm)	32.94 ± 5.02	9.39 ± 6.0	33.72 ± 4.6	8.54 ± 4.3	0.754	<0.001*	<0.001*
Elastic Modulus (N/mm2)	6582.70 ± 1150.7	490.80 ± 303.1	5999.99 ± 1166.7	1170.71 ± 503.2	0.157	<0.001*	<0.001*
Ultimate Stress (N/mm2)	152.07 ± 22.01	88.60 ± 41.4	153.46 ± 25.8	148.06 ± 31.7	0.002*	<0.001*	0.748
Yield Stress (N/mm2)	121.60 ± 12.1	61.89 ± 31.7	130.64 ± 13.3	101.27 ± 29.0	0.032*	0.002*	0.040*

Table 5. Correlations between immune factors and healing outcomes

Time Point	Biomarker	Healing Factor	R	p-value
Hour 1 (Blood)	CD25+ T cells	Ultimate stress (N/mm2)	-0.562	0.036
	CD25+ T cells	Max Force (N)	-0.547	0.043
	CD8 T cells	Max Force (N)	0.544	0.044
	IL-6	Ultimate stress (N/mm2)	-0.832	0.040
	MIG (CXCL9)	Max Force (N)	-0.810	0.051
Day 1 (Blood)	All T cells	Ultimate stress (N/mm2)	0.707	0.005
	All T cells	Max Force (N)	0.670	0.001
	CD25+ T cells	Ultimate stress (N/mm2)	-0.593	0.026
	DN T cells	Ultimate stress (N/mm2)	-0.577	0.031
	B cells	Ultimate stress (N/mm2)	-0.569	0.034
	Neutrophils	Ultimate stress (N/mm2)	0.540	0.046
	Monocytes	Ultimate stress (N/mm2)	-0.536	0.048
	Monocytes	Max Force (N)	-0.529	0.052
	CD25+ T cells	Max Force (N)	-0.525	0.055
	MIG (CXCL9)	Max Force (N)	-0.886	0.003
	IL-9	Max Force (N)	-0.756	0.030
	Eotaxin	Max Force (N)	-0.748	0.033
	IL-6	Max Force (N)	-0.714	0.047
Day 3 (Blood)	Neutrophils	Ultimate stress (N/mm2)	0.549	0.042
	LIF	Stiffness (N/mm)	0.986	0.014
	LIF	Elastic Modulus (N/mm2)	0.970	0.030
Day 7 (Blood)	Monocytes	Max Force (N)	-0.614	0.020
	Neutrophils	Max Force (N)	0.588	0.027
	Neutrophils	Ultimate stress (N/mm2)	0.586	0.028

	Monocytes	Ultimate stress (N/mm2)	-0.530	0.051
	MIP-1α	Elastic Modulus (N/mm2)	0.970	0.001
	MIP-1α	Stiffness (N/mm)	0.917	0.010
	IL-1α	Max Force (N)	0.833	0.040
	MIG (CXCL9)	Ultimate stress (N/mm2)	-0.719	0.045
	IL-1α	Stiffness (N/mm)	0.818	0.047
Day 14 (Blood)	CD8 T cells	Ultimate stress (N/mm2)	-0.628	0.017
	CD25+ T cells	Ultimate stress (N/mm2)	0.579	0.030
Day 21 (Blood)	Myeloid	Stiffness (N/mm)	-0.560	0.038
Day 21 (Callus)	CD4 T cells	Stiffness (N/mm)	-0.566	0.035
	M1 Mono	Ultimate stress (N/mm2)	-0.559	0.038
	M2 Mono	Ultimate stress (N/mm2)	0.559	0.038

REFERENCE

1 Holmes, D. Closing the gap. *Nature* **550**, S194-S195 (2017).

2 Schottel, P. C., O'Connor, D. P. & Brinker, M. R. Time trade-off as a measure of health-related quality of life: long bone nonunions have a devastating impact. *The Journal of Bone and Joint Surgery. American Volume* **97**, 1406 (2015).

3 Wildemann, B. *et al.* Non-union bone fractures. *Nature Reviews Disease Primers* **7**, 1-21 (2021).

4 Ekegren, C. L., Edwards, E. R., De Steiger, R. & Gabbe, B. J. Incidence, costs and predictors of non-union, delayed union and mal-union following long bone fracture. *International journal of environmental research and public health* **15**, 2845 (2018).

5 Cunningham, B. P., Brazina, S., Morshed, S. & Miclau III, T. Fracture healing: A review of clinical, imaging and laboratory diagnostic options. *Injury* **48**, S69-S75 (2017).

6 Weber, B. G. & Cech, O. in *Pseudarthrosis: pathophysiology, biomechanics, therapy, results* 323-323 (1976).

7 Andrzejowski, P. & Giannoudis, P. V. The 'diamond concept'for long bone non-union management. *Journal of Orthopaedics and Traumatology* **20**, 1-13 (2019).

8 Elliott, D. *et al.* A unified theory of bone healing and nonunion: BHN theory. *The bone & joint journal* **98**, 884-891 (2016).

9 Einhorn, T. A. & Gerstenfeld, L. C. Fracture healing: mechanisms and interventions. *Nature reviews. Rheumatology* **11**, 45-54 (2015). https://doi.org:10.1038/nrrheum.2014.164

10 Schottel, P. C., O'Connor, D. P. & Brinker, M. R. Time Trade-Off as a Measure of Health-Related Quality of Life: Long Bone Nonunions Have a Devastating Impact. *Journal of Bone and Joint Surgery-American Volume* **97a**, 1406-1410 (2015). https://doi.org:10.2106/Jbjs.N.01090

11 Wildemann, B. *et al.* Non-union bone fractures. *Nat Rev Dis Primers* **7**, 57 (2021). https://doi.org:10.1038/s41572-021-00289-8

12 Wolff, J. *The law of bone remodelling*. (Springer Science & Business Media, 2012).

13 FROST, H. 'Mass' and the 'mechanostat': a proposal. *Anat. Rec.* **219**, 1-9 (1987).

14 Perren, S. Physical and biological aspects of fracture healing with special reference to internal fixation. *Clinical orthopaedics and related research*, 175-196 (1979).

15 Claes, L. & Heigele, C. Magnitudes of local stress and strain along bony surfaces predict the course and type of fracture healing. *Journal of biomechanics* **32**, 255-266 (1999).

16 Loi, F. *et al.* Inflammation, fracture and bone repair. *Bone* **86**, 119-130 (2016). https://doi.org:10.1016/j.bone.2016.02.020

17 Cheng, A. *et al.* Early systemic immune biomarkers predict bone regeneration after trauma. *Proceedings of the National Academy of Sciences* **118** (2021).

18 Zondervan, R. L., Vorce, M., Servadio, N. & Hankenson, K. D. Fracture Apparatus Design and Protocol Optimization for Closed-stabilized Fractures in Rodents. *Journal of visualized experiments : JoVE* (2018). https://doi.org:10.3791/58186

19 Bonnarens, F. & Einhorn, T. A. Production of a standard closed fracture in laboratory animal bone. *Journal of orthopaedic research : official publication of the Orthopaedic Research Society* **2**, 97-101 (1984). https://doi.org:10.1002/jor.1100020115

20 Sweetwyne, M. T. & Murphy-Ullrich, J. E. Thrombospondin1 in tissue repair and fibrosis: TGF-β-dependent and independent mechanisms. *Matrix Biol* **31**, 178-186 (2012). https://doi.org:10.1016/j.matbio.2012.01.006

21 Zhu, W. *et al.* Ankylosing spondylitis: etiology, pathogenesis, and treatments. *Bone Research* **7**, 22 (2019). https://doi.org:10.1038/s41413-019-0057-8

22 Augat, P., Hollensteiner, M. & von Ruden, C. The role of mechanical stimulation in the enhancement of bone healing. *Injury* **52 Suppl 2**, S78-S83 (2021). https://doi.org:10.1016/j.injury.2020.10.009

23 Claes, L. E. *et al.* Effects of mechanical factors on the fracture healing process. *Clinical orthopaedics and related research*, S132-147 (1998). https://doi.org:10.1097/00003086-199810001-00015

24 Bansiddhi, A., Sargeant, T. D., Stupp, S. I. & Dunand, D. C. Porous NiTi for bone implants: a review. *Acta Biomater* **4**, 773-782 (2008). https://doi.org:10.1016/j.actbio.2008.02.009

25 Safranski, D., Dupont, K. & Gall, K. Pseudoelastic NiTiNOL in Orthopaedic Applications. *Shape Memory and Superelasticity* **6**, 332-341 (2020). https://doi.org:10.1007/s40830-020-00294-y

26 Bottlang, M. *et al.* Effects of construct stiffness on healing of fractures stabilized with locking plates. *The Journal of bone and joint surgery. American volume* **92 Suppl 2**, 12-22 (2010). https://doi.org:10.2106/jbjs.J.00780

27 Bottlang, M. & Feist, F. Biomechanics of Far Cortical Locking. *Journal of Orthopaedic Trauma* **25** (2011).

28 Ghiasi, M. S., Chen, J. E., Rodriguez, E. K., Vaziri, A. & Nazarian, A. Computational modeling of human bone fracture healing affected by different conditions of initial healing stage. *BMC Musculoskeletal Disorders* **20**, 562 (2019). https://doi.org:10.1186/s12891-019-2854-z

29 Steiner, M., Claes, L., Ignatius, A., Simon, U. & Wehner, T. Disadvantages of interfragmentary shear on fracture healing--mechanical insights through numerical simulation. *Journal of orthopaedic research : official publication of the Orthopaedic Research Society* **32**, 865-872 (2014). https://doi.org:10.1002/jor.22617

30 Barcik, J. *et al.* The absence of immediate stimulation delays bone healing. *Bone* **175**, 116834 (2023). https://doi.org:10.1016/j.bone.2023.116834

31 Windolf, M., Ernst, M., Schwyn, R., Arens, D. & Zeiter, S. The relation between fracture activity and bone healing with special reference to the early healing phase - A preclinical study. *Injury* **52**, 71-77 (2021). https://doi.org:10.1016/j.injury.2020.10.050

32 Augat, P. *et al.* Shear movement at the fracture site delays healing in a diaphyseal fracture model. *Journal of Orthopaedic Research* **21**, 1011-1017 (2003). https://doi.org:https://doi.org/10.1016/S0736-0266(03)00098-6

33 Coulis, G. *et al.* Single-cell and spatial transcriptomics identify a macrophage population associated with skeletal muscle fibrosis. *Science advances* **9**, eadd9984 (2023).

34 Yang, H. *et al.* Therapeutic potential of targeting membrane-spanning proteoglycan SDC4 in hepatocellular carcinoma. *Cell Death & Disease* **12**, 492 (2021).

35 Li, G. *et al.* Macrophage-secreted TSLP and MMP9 promote bleomycin-induced pulmonary fibrosis. *Toxicology and applied pharmacology* **366**, 10-16 (2019).

36 Yu, Q. & Stamenkovic, I. Cell surface-localized matrix metalloproteinase-9 proteolytically activates TGF-β and promotes tumor invasion and angiogenesis. *Genes & development* **14**, 163-176 (2000).

37 Reinke, S. *et al.* Terminally differentiated CD8+ T cells negatively affect bone regeneration in humans. *Science translational medicine* **5**, 177ra136-177ra136 (2013).

38 Hebb, J. H. *et al.* Bone healing in an aged murine fracture model is characterized by sustained callus inflammation and decreased cell proliferation. *Journal of Orthopaedic Research®* **36**, 149-158 (2018).

39 Baht, G. S., Vi, L. & Alman, B. A. The Role of the Immune Cells in Fracture Healing. *Curr Osteoporos Rep* **16**, 138-145 (2018). https://doi.org:10.1007/s11914-018-0423-2

40 Nicola, N. A. & Babon, J. J. Leukemia inhibitory factor (LIF). *Cytokine & growth factor reviews* **26**, 533-544 (2015). https://doi.org:10.1016/j.cytogfr.2015.07.001

41 Newman, H., Shih, Y. V. & Varghese, S. Resolution of inflammation in bone regeneration: From understandings to therapeutic applications. *Biomaterials* **277**, 121114 (2021). https://doi.org:https://doi.org/10.1016/j.biomaterials.2021.121114

42 Könnecke, I. *et al.* T and B cells participate in bone repair by infiltrating the fracture callus in a two-wave fashion. *Bone* **64**, 155-165 (2014).

43 Lybrand, K., Bragdon, B. & Gerstenfeld, L. Mouse Models of Bone Healing: Fracture, Marrow Ablation, and Distraction Osteogenesis. *Current Protocols in Mouse Biology* **5**, 35-49 (2015). https://doi.org:10.1002/9780470942390.mo140161

44 Histing, T. *et al.* Small animal bone healing models: standards, tips, and pitfalls results of a consensus meeting. *Bone* **49**, 591-599 (2011). https://doi.org:10.1016/j.bone.2011.07.007

45 Bartnikowski, M., Bartnikowski, N., Woloszyk, A., Matthys, R. & Glatt, V. Genetic variation in mice affects closed femoral fracture pattern outcomes. *Injury* **50**, 639-647 (2019). https://doi.org:10.1016/j.injury.2019.02.012

46 Patrick, M. D., Keys, J. F., Suresh Kumar, H. & Annamalai, R. T. Injectable nanoporous microgels generate vascularized constructs and support bone regeneration in critical-sized defects. *Scientific Reports* **12**, 15811 (2022). https://doi.org:10.1038/s41598-022-19968-x

47 Jepsen, K. J., Silva, M. J., Vashishth, D., Guo, X. E. & van der Meulen, M. C. H. Establishing Biomechanical Mechanisms in Mouse Models: Practical Guidelines for Systematically Evaluating Phenotypic Changes in the Diaphyses of Long Bones. *Journal of Bone and Mineral Research* **30**, 951-966 (2015). https://doi.org:https://doi.org/10.1002/jbmr.2539

48 Hao, Y. *et al.* Integrated analysis of multimodal single-cell data. *Cell* **184**, 3573-3587. e3529 (2021).

49 Ianevski, A., Giri, A. K. & Aittokallio, T. Fully-automated and ultra-fast cell-type identification using specific marker combinations from single-cell transcriptomic data. *Nature communications* **13**, 1246 (2022).

50 Franzén, O., Gan, L.-M. & Björkegren, J. L. M. PanglaoDB: a web server for exploration of mouse and human single-cell RNA sequencing data. *Database* **2019** (2019). https://doi.org:10.1093/database/baz046

51 Jin, S. *et al.* Inference and analysis of cell-cell communication using CellChat. *Nature communications* **12**, 1088 (2021).